ELSEVIER

Wear 251 (2001) 1265–1278

WEAR

www.elsevier.com/locate/wear

Finite element modelling of crack growth and wear particle formation in sliding contact

P.L. Ko [a,*], S.S. Iyer [b], H. Vaughan [c], M. Gadala [c]

[a] *National Research Council of Canada, Innovation Centre, 3250 East Mall, Vancouver, BC, Canada V6T 1W5*
[b] *Babcock & Wilcox Canada Ltd., Cambridge, Ont., Canada N1R 5V3*
[c] *Department of Mechanical Engineering, University of British Columbia, Vancouver, BC, Canada V6T 1Z4*

Abstract

Two steel surfaces in sliding contact are examined analytically and experimentally. The experiments are restricted to the reciprocating sliding of a relatively hard circular cylinder on a soft plane but the analytical model developed can be applied to general two-dimensional sliding contact situations. The surfaces are nominally smooth (smooth to the touch) but microscopic roughness is modelled as surface asperities having the form of randomly spaced cylindrical corrugations, which ideally represent plane strain conditions perpendicular to the direction of sliding. Under dry sliding conditions (high friction) it is known that crack growth and particle detachment can occur below the elastic limit. By applying finite element methods to linear elastic fracture mechanics, a model is developed, which simulates crack growth and wear particle detachment from an existing surface crack. A range of mixed mode stress intensity factors for cyclic loading is evaluated and related to crack extension by a Paris type equation. The maximum tensile stress criterion is used to determine the crack-turn-angle (crack path) during crack propagation under cyclic loading. It is found that eventually the crack extends and turns toward the surface of the plane to form a single wear particle. Estimated wear volume is calculated using surface statistics and integration. The predicted particle size and the estimated wear volume are in reasonable agreement with those obtained from experiments involving hardened steel sliding on steel. Some of the tested specimens were sectioned and examined in a scanning electron microscope. Two distinct types of crack were observed. Hardness tests on the section revealed significant work hardening in the near-surface layer.

Keywords: Finite element; Fracture mechanics; Crack propagation; Wear modelling

1. Introduction

The existence of microscopic surface and subsurface cracks, and subsurface voids in metal components is well documented [1]. During sliding between two metals, the forced contact between the two sets of surface asperities produces local elastic–plastic deformation and extension of the microscopic cracks. Repeated cyclic loading can cause cumulative crack extension leading eventually to the formation of slivers, platelets and particles, some of which are removed from the surfaces as wear particles, while others are trapped at the interface and formed into a particle layer on one of the surfaces.

In an earlier paper by two of the authors [2], an investigation into wear particle formation was conducted for hardened steel sliding on martensitic grade stainless steel in a unidirectional sliding motion with 2 mm stroke length. The wear scar formation and its boundary shape were followed from the initial few sliding strokes to tens of thousands of repeated cycles. Results of these detailed studies revealed that during the first few cycles of contact, extensive geometrical change occurs in the contact area either by a continuous indentation mechanism or by a relatively coarse delamination mechanism, primarily influenced by the lubrication conditions at the interface. Under the indentation mechanism, scar size continues to expand and particle formation occurs by fine delamination and fracture of small roughness features within the scar. In the case of coarse delamination, particle formation begins with the initial geometry deformation and evolves into a delamination mechanism as the expansion of scar size slows down.

Under wet sliding conditions, wear debris trapped in the contact zone is more prone to be pulverised and compacted into a smooth and continuous third body layer covering the wear scar. In some situations, this layer protects the softer surface but continues to wear the much harder counter part. Jahanmir [3] observed several wear mechanisms in wear tests using friction-reducing additives in the base oil. He attributed wear at low friction level ($\mu = 0.05$–0.1) to mild surface deformation, at intermediate level (0.15–0.25) to plowing and delamination, and at high friction level

* Corresponding author. Tel.: +1-604-221-3071; fax: +1-604-221-3088.
E-mail address: pak.ko@nrc.ca (P.L. Ko).

0043-1648/01/$ – see front matter
PII: S0043-1648(01)00780-3

(0.35–0.65) to adhesion and severe delamination. The experimental observations reported in [2,3] reinforce the notion that different wear models are needed for different loading and frictional conditions.

Models of crack propagation and particle formation based on fracture mechanics have been developed by researchers in wear studies. Hanson and Keer [4] developed contact fatigue models to show that, at high stresses, crack propagation is the dominant wear mechanism. Advances in computational techniques and computer hardware have also stimulated promising work on numerical and finite element models of asperity contact stresses and strains [5,6], and models of crack growth in conjunction with fatigue and fracture mechanics concepts [7–9]. While many researchers used mode I tensile stresses for subsurface crack propagation, others used the mode II criterion [10]. Comninou [11], Keer et al. [12] and Sheppard et al. [13] calculated stress intensity factors in modes I and II for horizontal cracks in the subsurface. Keer and Bryant [14] and Bower [15] analysed cracks that were inclined to the surface and calculated the resulting stress intensity factors. Earlier, Erdogan and Sih [16] and Sih [17] established the criteria for the determination of angles of crack growth under mixed mode conditions. Bower [15] succeeded in predicting the angle of crack extension of a lubricated crack. In most of these analyses, a priori assumption concerning the mode of fracture, mode I or mode II, is required.

In the present paper, a wear model that can be applied to severe contact sliding situations with high coefficients of friction is presented. The analysis applies fracture mechanics to a finite element model to predict wear particle formation in the elastic state. In particular, no prior assumption about the relative importance or presence of modes I and II fracture is required.

2. Model development

Surface statistics is used to quantify the two engineering surfaces in contact. A finite element model using the FE code ANSYS is developed for the contact of an equivalent cylindrical asperity with an elastic half-space. The contact between the asperity and the half-space is established through special types of contact elements. The mechanical response quantities such as deformations, strains and stresses are calculated for several cycles of reciprocating sliding under various friction and normal load levels. The cyclic strain components of the surface elements of the half-space are tracked through the loading cycles.

Even though it was established in [2] that wear, for high load and friction conditions, is accompanied by geometric (plastic) deformation in the near-surface layer, the authors have chosen to base their theory on linear elastic fracture mechanics and Hertzian contact theory. There are three main reasons for this approach. Firstly, linear elastic fracture mechanics has been used with confidence to predict fracture strength of engineering components for many decades. The stress singularity and associated local plastic deformation at the crack tip does not affect the accuracy of the theoretical prediction of a failure load if the correct stress intensity factor is used. Secondly, it is of interest to know whether a microscopic model based on linear theories, backed by finite elements, and using recent analytic formulas for fracture under mixed mode loading, can also yield reliable information about the wear process of metals. Thirdly, the inclusion of plasticity theory in the numerical work would require a major extension of that part of the investigation and conceal the significance of elasticity. It is shown later, by comparing the numerical results with same carefully tested specimens that the use of the simplistic method is justified and the omission of plasticity is not detrimental in predicting wear particle geometry and size. One of the authors, Gadala, is pursuing a non-linear elastoplastic analysis for the same problem with the aid of the critical parameters identified from the present analysis.

2.1. Assumptions

To minimise the mathematical complexities in the finite element analysis, it is assumed that the discrete contact zones are sufficiently separated so that they do not interact with each other. It is further assumed that only one asperity, which is idealised as a cylinder, Fig. 1, will come into contact with the semi-infinite half-space in the sliding direction. A mixed mode (modes I and II) stress intensity factor solution is developed for general crack geometry using finite element methodology.

Later, the model assumes the existence of a surface crack in the elastic half-space and studies crack growth for the cyclic Hertzian loading. The crack propagation direction is calculated based on a maximum tensile stress criterion rather than assuming the direction to be parallel to the sliding direction as in some other studies. When the crack re-emerges at the surface, it detaches from the parent surface to form a wear particle.

2.2. Finite element model and boundary conditions for dry sliding wear

A three-node "Contact48" element [ANSYS] is applied in a plane strain configuration that represents the contact

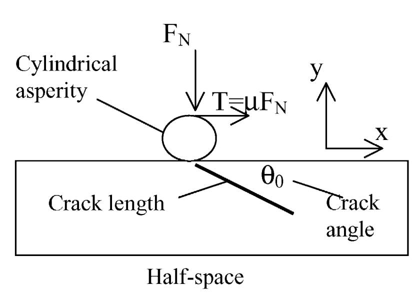

Fig. 1. Schematic diagram of contact model.

between the asperity and the half-plane. The application of this type of element results in precise tracking of contact nodes and surfaces at any given time. By measuring the relative displacement of the nodes on the crack surfaces, the procedure gives clear and unambiguous information about the opening and sliding of the crack surfaces. The entire loading history is broken into several load steps and sub-steps (or sub-load steps) to facilitate convergence of the solution. For instance, the first load step, which involves only the indentation of the asperity on the half-space, is performed using 20 sub-steps.

A surface crack in the plane is introduced into the finite element model and crack growth is computed. The crack face displacements in both opening and sliding modes are related to the stress intensity factors for modes I and II fracture. The change in the stress intensity factors for a given load cycle is evaluated and related to crack growth through a proposed 'Paris' type law [18]. The model shows that the direction of crack propagation changes with each cycle of loading and will eventually 'emerge' at the free surface of the plane to form a wear particle.

During the intermediate stage when the crack is growing incrementally, the crack tip is subjected to varying amounts of modes I and II displacements. The finite element analysis will show later that the mode II stress intensity factor is the predominant one for the crack geometry examined here.

2.3. Determination of stress intensity factors

The stress intensity factors K_{I} and K_{II} are calculated from the displacement field at the crack tip. The equations for the displacement field (u, v) surrounding the crack tip under plane strain conditions expressed in polar co-ordinates (r, θ) can be found in text books and are given by

$$u = \frac{K_{\mathrm{I}}}{4G}\sqrt{\frac{r}{2\pi}}\left[(2\lambda-1)\cos\frac{\theta}{2} - \cos\frac{3\theta}{2}\right] - \frac{K_{\mathrm{II}}}{4G}\sqrt{\frac{r}{2\pi}}\left[(2\lambda+3)\sin\frac{\theta}{2} + \sin\frac{3\theta}{2}\right] + \mathrm{HOT} \quad (1a)$$

$$v = \frac{K_{\mathrm{I}}}{4G}\sqrt{\frac{r}{2\pi}}\left[(2\lambda-1)\sin\frac{\theta}{2} - \sin\frac{3\theta}{2}\right] - \frac{K_{\mathrm{II}}}{4G}\sqrt{\frac{r}{2\pi}}\left[(2\lambda+3)\cos\frac{\theta}{2} + \cos\frac{3\theta}{2}\right] + \mathrm{HOT} \quad (1b)$$

where $\lambda = 3$–4υ, υ is the Poisson's ratio and G is the shear modulus.

The origin of the co-ordinates is at the crack tip and the crack faces are at $\theta = \pm 180^\circ$. Thus, the relative change in position of two particles originally in contact but on opposite faces of the crack can be found by evaluating u and v at $\theta = \pm 180^\circ$. We obtain

$$|\Delta u| = \frac{K_{\mathrm{II}}}{G}\sqrt{\frac{r}{2\pi}}(1+\lambda) + \mathrm{HOT} \quad (2a)$$

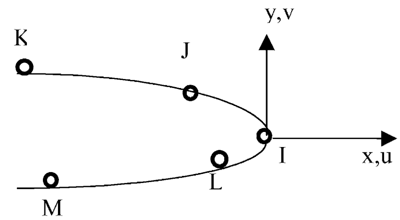

Fig. 2. Co-ordinate system at crack tip for displacement calculation.

$$|\Delta v| = \frac{K_{\mathrm{I}}}{G}\sqrt{\frac{r}{2\pi}}(1+\lambda) + \mathrm{HOT} \quad (2b)$$

Fig. 2 shows five node points I, J, K, L and M with I at the crack tip. When the crack is closed, K and M are in contact, as are J and L. When the crack is opened, the relative displacements $|\Delta u|$ and $|\Delta v|$ between K and M, and J and L, are given by Eqs. (2a) and (2b), using the appropriate values of r.

Four constants, A, B, C and D are introduced in the expressions for Δu and Δv at the nodes J and K; thus

$$\frac{|\Delta v|}{\sqrt{r}} = A + B\sqrt{r} + \mathrm{HOT}; \qquad \frac{|\Delta u|}{\sqrt{r}} = C + D\sqrt{r} + \mathrm{HOT} \quad (3)$$

Obtaining numerical values for Δu and Δv at J and K, with known numerical values of r, enables the four constants A, B, C and D to be determined numerically. Noting that "A" is the limit of $|\Delta v|/\sqrt{r}$ as $r \to 0$, it follows from Eqs. (2b) and (3) that

$$K_{\mathrm{I}} = \sqrt{2\pi}\,\frac{GA}{1+\lambda} \quad (4a)$$

Similarly from Eqs. (2a) and (3), it follows that:

$$K_{\mathrm{II}} = \sqrt{2\pi}\,\frac{GC}{1+\lambda} \quad (4b)$$

Thus, K_{I} and K_{II} are determined from the known values of A and C.

2.4. Fracture and crack-turn-angle for mixed mode loading

The basis of the model for crack growth and wear particle formation used in this paper is that at each cycle of loading, the relative amounts of modes I and II displacements at a crack tip change with each cycle. These relative changes are accompanied by a corresponding change in the direction of the incremental crack growth. For pure mode I displacements, an existing crack will propagate forward with no change in direction. For pure mode II displacements, an existing crack will turn with a sharp corner, making a turn angle of 70°; at a value of K_{II} equal to $(\sqrt{3}/2)K_{\mathrm{IC}}$; see for example the analytical and experimental work of Vaughan [19]. For general combinations of modes I and II displacements, which are anticipated in the wear particle problem, it is necessary to be able to predict the fracture load and the fracture angle for random loading conditions. Using the maximum tensile stress criterion (MTS), Vaughan [20] has shown that a parabolic fracture locus may be used, given by

$$4\left(\frac{K_{\mathrm{II}}}{K_{\mathrm{IC}}}\right)^2 + 3\left(\frac{K_{\mathrm{I}}}{K_{\mathrm{IC}}}\right) - 3 = 0 \tag{5}$$

where K_{I} and K_{II} are the stress intensity factors and K_{IC} is the fracture toughness obtained from a mode I test. Thus, fracture will occur when K_{I} and K_{II} satisfy Eq. (5). Associated with Eq. (5) is a propagation angle θ^*, or turn angle, defining the new crack-path direction. This angle θ^* is used in our wear particle model even though fracture has not yet occurred, that is, during the crack growth phase. The angle θ^* (°) is given by

$$\theta^* = 105\left(\frac{K_{\mathrm{II}}}{K_{\mathrm{IC}}}\right) - 32\left(\frac{K_{\mathrm{II}}}{K_{\mathrm{IC}}}\right)^3 \tag{6}$$

Eq. (6) is obviously a curve-fit to a numerical solution of a transcendental equation. We note that for pure mode I loading, $K_{\mathrm{II}} = 0$ and $\theta^* = 0$, that is, the crack path does not turn. For pure mode II loading, $K_{\mathrm{I}} = 0$ and so from Eq. (5), fracture occurs when $K_{\mathrm{II}} = (\sqrt{3}/2)K_{\mathrm{IC}}$, giving $\theta^* = 105(\sqrt{3}/2) - 32(\sqrt{3}/2)^3 = 70.1°$. The exact solution is $\theta^* = \cos^{-1}(1/3) \approx 70.5°$.

Eqs. (5) and (6) have been derived analytically in [20] and also verified experimentally. The experiments, about 90 in total, were conducted on plexiglas discs and showed remarkable consistency and accuracy with the formulas. It is realised that metals may not behave in fracture like the plexiglas reported in [20], however, recent experiments conducted by Magill and Zwerneman on steel plates [21] show a close similarity when Eqs. (5) and (6) are applied to their results. For these reasons, the authors feel justified in using Eq. (6) to predict the step-wise crack path for the changing values of K_{I} and K_{II}, which occur as the wear particle is created, the values of K_{I} and K_{II} being known at each stage from Eqs. (4a) and (4b).

2.5. *Crack growth rate for mixed mode loading*

For a growing crack under a constant amplitude cyclic stress intensity, if the miniscule plastic zone at the crack tip is contained by the surrounding elastic singularity zone, the conditions at the crack tip are defined by the current value of 'K' at every instant. The crack growth depends on $\Delta K = (K_{\max} - K_{\min})$. The influence of the plastic zone is implicit in ΔK since the zone is controlled by $K_{\max}$ and $K_{\min}$.

Fatigue crack growth in metal is usually estimated by using the following relationship due to Paris and Erdogan [18]:

$$\frac{\mathrm{d}c}{\mathrm{d}N} = C(\Delta K)^m \tag{7}$$

where $\mathrm{d}c/\mathrm{d}N$ is the crack growth per cycle, ΔK the stress intensity factor increment, C and m are material constants to be found experimentally. The constant m was assigned a value of 4 by Paris and Erdogan [18] but may vary from 2 to 7 for different materials [22].

For crack growth due to mixed modes I and II cyclic loading, an effective mixed mode stress intensity factor, ΔK_{eff} is often used. Tanata [23] used the relationship

$$\Delta K_{\mathrm{eff}} = [\Delta K_{\mathrm{I}}^4 + 8\,\Delta K_{\mathrm{II}}^4]^{1/4} \tag{8}$$

Eq. (8) has been used in Eq. (7) in this paper to evaluate crack growth rates.

3. Finite element analysis

3.1. *Problem definition*

The finite element model simulates the effect of hard asperities loaded against a softer surface that contains an inherent defect in the form of a surface crack, deforming elastically so that the axioms of linear elastic fracture mechanics can be applied. For modelling purposes, a cylinder of 10 mm in diameter with an axial length of 12.7 mm is used as the upper sliding surface. The surface finish of the cylinder is ground finish (asperities having a radius of curvature of approximately 1 mm). The cylinder slides over the flat surface of a disc 19 mm in diameter and 5 mm thick. The surface of the disc has the same ground finish as the cylinder. The two components are loaded in the normal direction for a range of normal forces up to 800 N. It should be noted that the normal loads are expressed in terms of load per unit length, which is 12.7 mm in the present case.

The material properties of type SAE 410 steel (E = 207 GPa; $\upsilon = 0.3$) are used for the upper surface. The lower surface is assumed to be an elastic semi-infinite half-space with an inherent surface defect, for example, a crack of 30 μm in length inclining at 45° from the contact surface. The density of asperities on the surface is taken as 10 mm^{-2}. The coefficient of friction μ for the analysis is taken to be 0.8 (a rather high value, nevertheless, it was experimentally observed under similar dry test conditions).

3.2. *Finite element results*

Fig. 3 illustrates the assumption of the initial crack of a specific length and orientation and the crack growth due to the cyclic contact loading. The co-ordinates of crack growth determines the cross-sectional area of the wear particle, and due to the assumption of the plane strain conditions, the third-dimension is simply the length of the cylinder.

Fig. 4(a) and (b) show the finite element mesh and crack growth pattern perpendicular to the first principal stress. For each load step, the stress intensity factors are evaluated from Eqs. (4a) and (4b). The Paris Law, Eq. (7), is used for calculating '$\mathrm{d}c$', the crack extension and the increase in total crack length for a fixed cyclic loading.

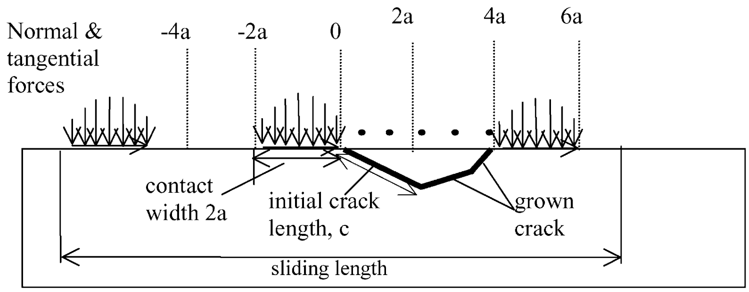

Fig. 3. Schematic diagram of moving load and crack growth.

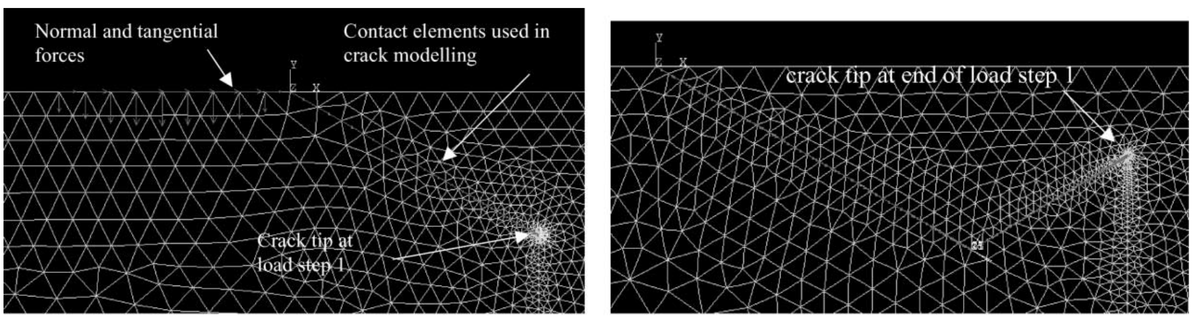

(a) (b)

Fig. 4. Fracture mechanics model with embedded crack. The crack faces are modelled with contact elements to detect contact between the crack faces and prevent the meshes from overlapping: (a) finite element model for crack growth; (b) crack faces modelled with contact elements.

There is an important simplification used in the calculation of ‘dc’ and N which is based upon experimental observation. It is shown in [20] that under repeated loads, which are high enough to cause crack growth, it is the first load only, which causes the major change in the subsequent crack-path direction. Later loads merely extend the path with secondary changes in the path direction. Thus, in the numerical work we deal with just two load steps. Load step 1 is defined as the number of cycles required to extend a crack by 50% of its original length. The first load only, determines the crack-path direction using Eq. (6). The path is then assumed to hold for all the remaining loads of load step 1 and “N” is calculated from Eq. (7) using ‘dc’ $= c/2$. Load step 2 is the number of cycles required to extend the crack to the surface, thus creating a wear particle. A new angle is calculated for load step 2 using Eq. (6) but as will be shown, there is little departure from that associated with load step 1, in accordance with the work reported in [20].

Table 1
Crack growth and particle formation vs. entry angle[a]

Initial crack orientation (step)	ΔK (MPa m$^{1/2}$)		dc_1 and dc_2 (μm)	dθ_i (°)	N (cycles)	Aspect ratio	Mass of particle (mg)
	ΔK_{I}	ΔK_{II}					
15 (1)	0.18	3.89	N/A	70	N/A	N/A	
15 (2)	N/A	N/A	N/A	N/A	N_2 = N/A	N/A	No particle
20 (1)	0.21	4.77	N/A	70	N/A	N/A	
20 (2)	N/A	N/A	N/A	N/A	N_2 = N/A	N/A	No particle
25 (1)	0.252	6.15	15	70	$N_1 = 116$	–	
25 (2)	0.66	7.91	2.27	69	$N_2 = 6$	2.91	0.049
30 (1)	0.297	6.4	15	69	$N_1 = 105$	–	
30 (2)	2.31	7.51	5.7	65	$N_2 = 18$	2.42	0.06
35 (1)	0.33	7.03	15	69	$N_1 = 78$	–	
35 (2)	3.57	6.86	8.9	62	$N_2 = 40$	2.1	0.072
40 (1)	0.36	7.47	15	69.5	$N_1 = 65$	–	
40 (2)	3.63	6.26	11.9	59	$N_2 = 53$	1.9	0.083
45 (1)	0.396	7.92	15	69	$N_1 = 55$	–	
45 (2)	3.63	5.6	N/A	59	N_2 = N/A	N/A	No particle

[a] Crack length: 30 μm, normal force: $P_{\mathrm{N}} = 800$ N, shear force: $F = 640$ N.

3.2.1. Finite element analysis of a crack with different entry angles

A typical crack 30 μm long with an initial orientation at 15, 20 and so on up to 45° to the surface was chosen as an example for the analysis. In the linear elastic analysis, the normal contact pressure and shear stress were applied on the disc and allowed to slide along the surface passing over the crack. Table 1 gives the numerical values obtained for the stress intensity factors and the crack-turn-angle for two load steps. These results show that the mode II stress intensity factor is predominant during the first load step in mixed mode fracture. In the second load step, the mode I stress intensity factor shows a significant increase while only a slight increase for the mode II factor. The latter actually decreases in the second load step for crack entry-angles equal to and greater than 35°. By 45° the mode II factor has gone below the threshold value of 6 MPa, inhibiting further crack growth.

Two examples of finite element output are shown in Fig. 5(a) and (b) for entry crack angles 25 and 45°, respectively. A close examination of the case for the 30° entry-angle, Table 1 and Fig. 5(c) and (d), shows the number of cycles are 105 and 18 for load steps 1 and 2, respectively. Graphically, Fig. 5(e) shows that the crack extended 15 μm during the first load step and 2.27 μm during the second

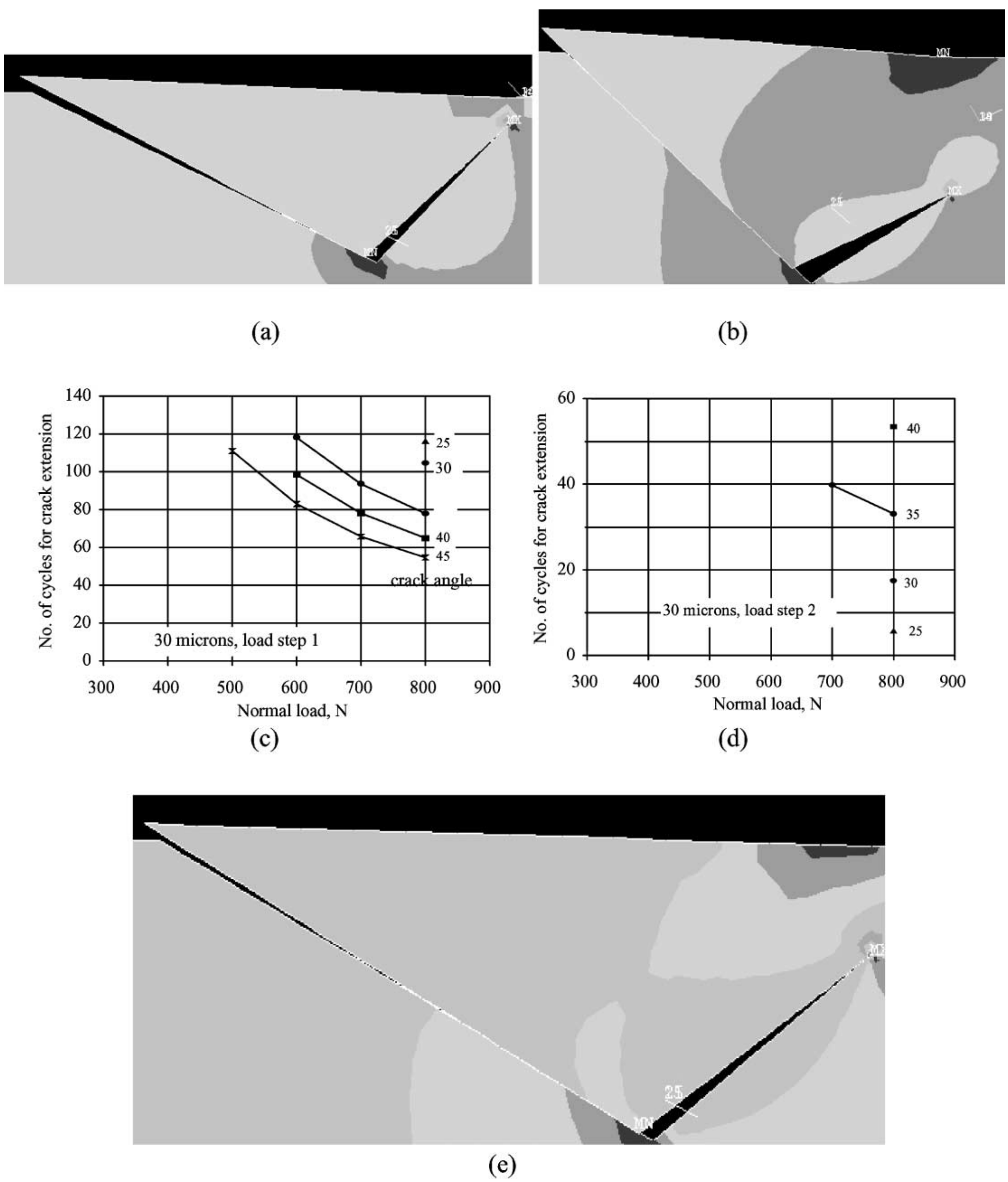

Fig. 5. Crack extension and maximum tensile stress (σ_θ) in the vicinity of the crack tip for a crack with an initial length of 30 μm: (a) $\theta = 25°$; (b) $\theta = 45°$; (c) load step 1; (d) load step 2; (e) $\theta = 30°$.

load step. During one cycle of sliding the SIFs at the crack tip vary as the normal and tangential pressure distributions, a profile with width $2a$, where a is the semi-contact width of the equivalent cylindrical asperity, move along the half-space containing the crack. When the profile is $(-3a, -a)$ from the opening of the crack, K_I attains a low value of $0.164\,\mathrm{MPa\,m^{1/2}}$ and K_{II} has a value of $5\,\mathrm{MPa\,m^{1/2}}$. As the pressure profile moves towards the crack by a distance 'a', i.e. at $(-2a, 0)$, K_{II} reaches its maximum value of $6.4\,\mathrm{MPa\,m^{1/2}}$ and K_I has a value of $0.297\,\mathrm{MPa\,m^{1/2}}$. This is the critical position of the loading cycle where K_{II}, the dominant SIF, attains its maximum value. When the pressure profile moves past, the crack opening on the surface, i.e. at $(0, 2a)$, the value of K_{II} falls to 2 whereas K_I increases to $2.1\,\mathrm{MPa\,m^{1/2}}$. As the load moves further away from the crack opening, K_{II} continues to fall rapidly while the value of K_I also decreases but more gradually. When the load is at $(3a, 5a)$, the values of both SIFs fall below $1\,\mathrm{MPa\,m^{1/2}}$ and they can no longer sustain crack growth. In load step 2, the maximum SIFs are reached when the load is at $(2.2a, 4.2a)$ from the crack opening on the surface during the returning half-cycle.

The finite element outputs also revealed that except for a very small section, about two to three elements of several micrometer in length and far away from the crack tip, the entire length of the bent crack face was stress-free. This observation confirmed that due to the effects of the mixed mode there was no real contact between the crack faces, except for that very small section away from the crack tip.

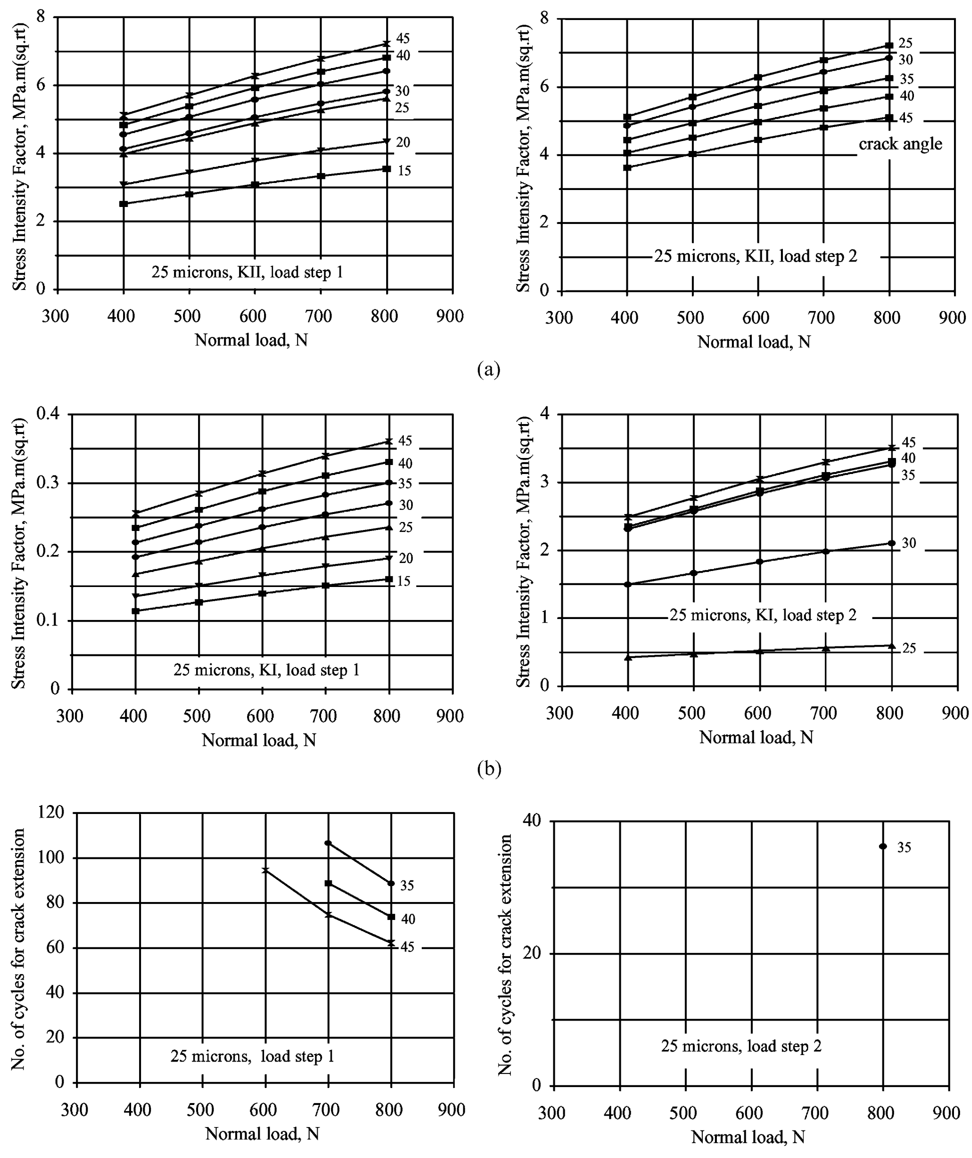

Fig. 6. The effect of normal load and crack angle on the stress intensity factors and number of cycles for crack growth, for a crack with an initial length of 25 μm: (a) for K_{II}, load steps 1 and 2; (b) for K_I, load steps 1 and 2; (c) number of cycles for crack extension.

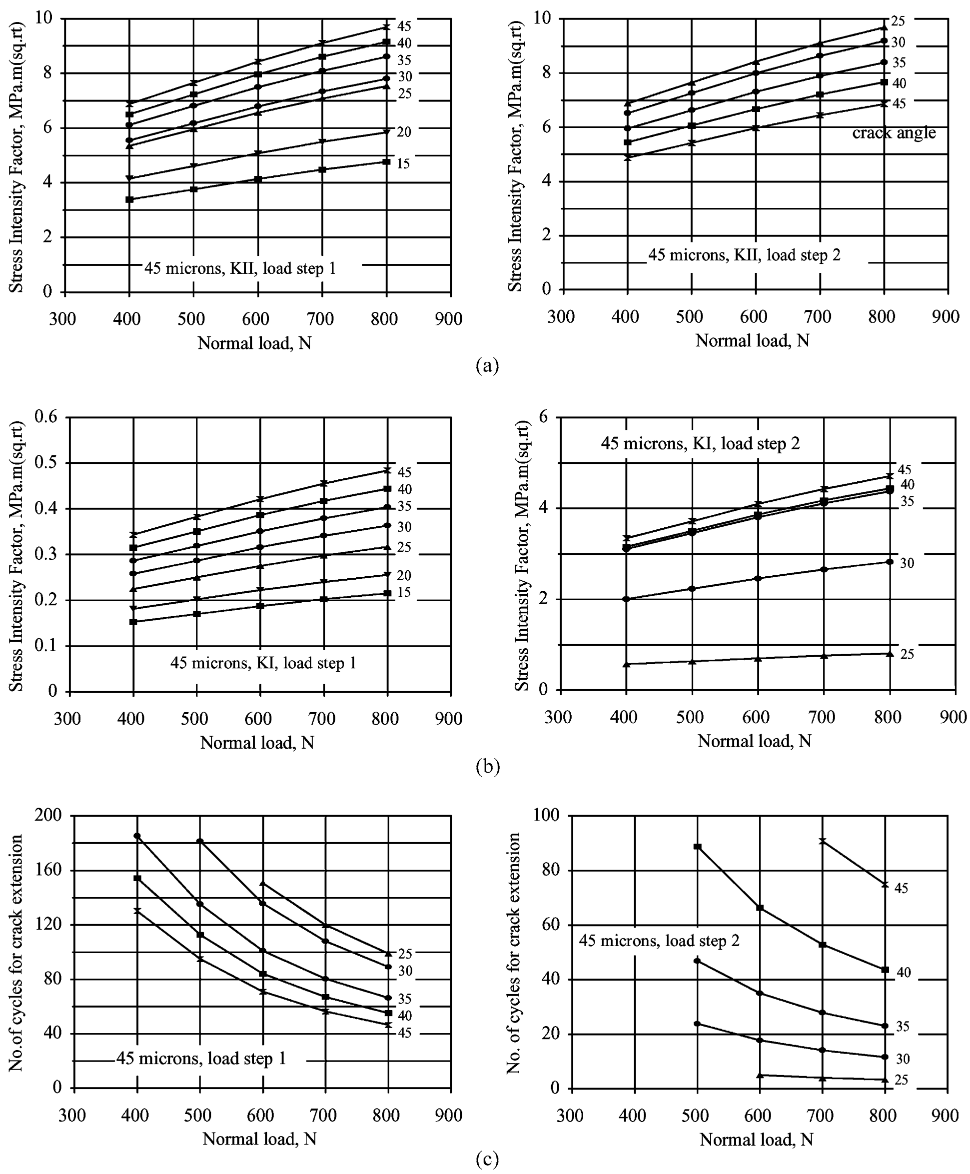

Fig. 7. The effect of normal load and crack angle on the stress intensity factors and number of cycles for crack growth, for a crack with an initial length of 45 μm: (a) for K_{II}, load steps 1 and 2; (b) for K_I, load steps 1 and 2; (c) number of cycles for crack extension.

3.2.2. Effects of loading and crack length

The stress intensity factors were calculated for a range of crack lengths (15–50 μm) and crack entry angles (15–45°) for normal loads 400–800 N. In general, the stress intensity factors increase with increasing normal load and crack length. The results of two crack lengths: 25 and 45 μm, were plotted in Figs. 6 and 7. The plots illustrate the general trend of the stress intensity factors K_I and K_{II} for load steps 1 and 2. The trend is similar to that described in detail in the previous section.

3.2.3. Formation of wear particles

The number of cycles for crack extension in each load step is calculated from Eqs. (7) and (8). Again, the results of this calculation are shown in Fig. 6(e) and (f) and Fig. 7(e) and (f) for the two crack lengths: 25 and 45 μm. For crack lengths shorter than 25 μm, the stress intensity factors calculated for the entire load range (up to 800 N) and entire range of entry angles (15–45°) are below the threshold value, that is, there is no crack extension. For crack lengths equal to and above 25 μm, the number of cycles needed for crack extension decreases as the normal load is increased. It is

Table 2
Experimental mass loss results of disc specimens (mg)

Normal load (N)	Number of sliding cycles			
	35 HRC		45 HRC	
200	0.15	0.3	0.15	3.05
300	0.15	0.275	0.42	2.12

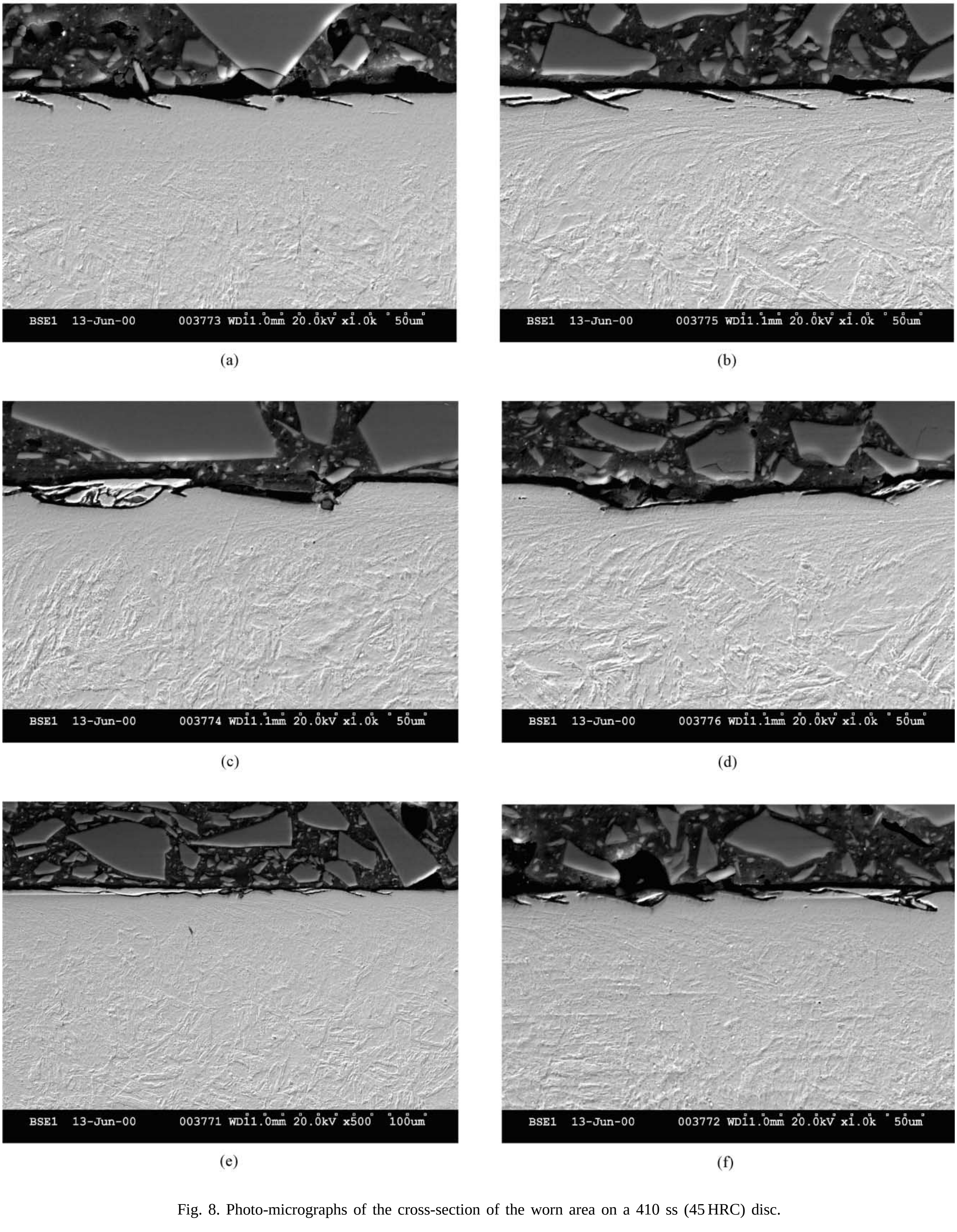

Fig. 8. Photo-micrographs of the cross-section of the worn area on a 410 ss (45 HRC) disc.

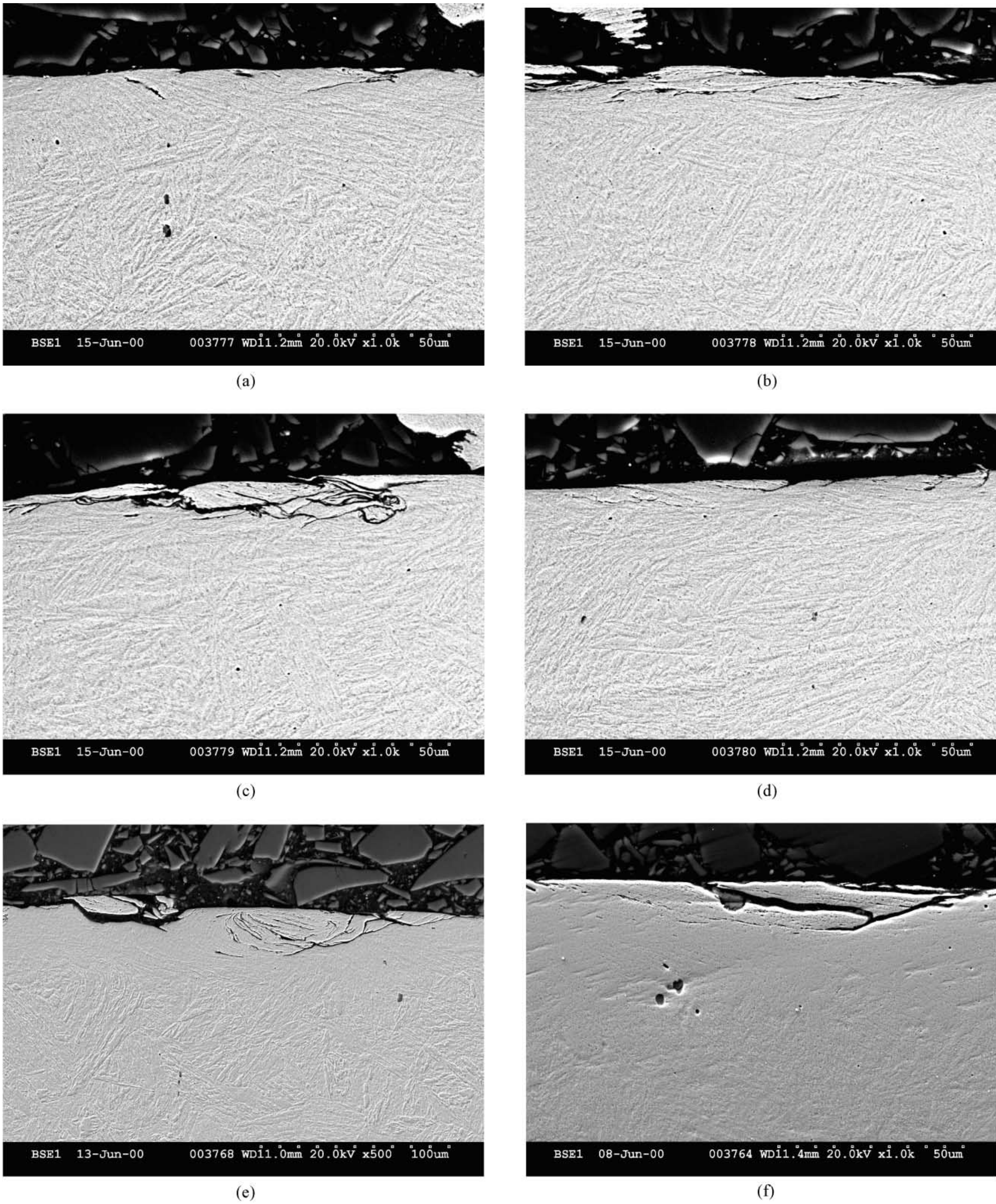

Fig. 9. Photo-micrographs of the cross-section of worn area on a 410 ss (35 HRC) disc showing both triangular and sliver particles.

noted that the number of cycles in load step 2 does not follow a regular pattern. This is because, in some cases, the extension from load step 2 reaches the surface before the next cycle calculation is needed.

4. Experimental

4.1. Test rigs and test procedures

A Cameron–Plint reciprocating sliding wear test rig was used for the dry sliding tests. The disc specimens were cut from SAE 410 stainless steel rod 22.2 mm in diameter with hardness 35 HRC. Some of these disc specimens were heat treated to 45 HRC. All specimens were cut to 2.5 mm thickness. One side of the disc was ground and polished to $R_a = 1\,\mu m$. The upper (dynamic) specimen was prepared from a carbon steel bar machined to 19 mm in diameter and cut to a length of 12.7 mm. It was hardened to 55 HRC and polished to $R_a = 1\,\mu m$. Dry sliding tests were carried out with normal loading of 200 and 300 N for 60 and 720 cycles.

The specimens were cleaned in an ultrasonic bath and weighed before and after each test. All tests were repeated once.

4.2. Experimental results

The results in Table 2 are the average mass losses of two duplicate tests. They show that after 60 cycles, the mass losses are negligibly small. Interestingly, after 720 cycles, the softer discs resulted in lower mass loss than the harder discs indicating a different wear mechanism might have occurred. The hardened discs could have more micro-cracks on the surface and subsurface resulting in the formation and detachment of larger particles.

4.3. Metallography examinations

Crack propagation and the formation of wear particles are of primary interest in the present study. Several worn discs were sectioned along the middle of the wear scar, polished and examined in the scanning electron microscope. Fig. 8 shows a series of photo-micrographs taken from a sectioned 45 HRC disc, which have been subjected to 300 N normal loading for 720 cycles. Several micro-cracks, 10–15 μm in length, can be seen in Fig. 8(a) and (b). The two micrographs in the middle, Fig. 8(c) and (d), reveal triangular voids near the surface that were likely created after particles had detached from the surface. The dimensions of these particles (voids) appear to have the same magnitude used in and predicted by the finite element model. Other types of wear particles in the form of thin slivers were also observed and are shown in the bottom two photo-micrographs of Fig. 8. Two other specimens from the 35 HRC discs that had been subjected to the same test conditions were also sectioned and examined. The photo-micrographs of Fig. 9 reveal many cracks that are thinner and longer than those observed in Fig. 8. These fine cracks appear to form along grain boundaries and follow the shear-flow directions. Particles formed from these cracks tend to be elongated and thinner. Nevertheless, large particles similar in appearance to those observed on a harder disc (Fig. 8) were also found, even though less prominent, in some locations in the softer material along the sectioned worn area, Fig. 9(e) and (f).

The etched cross-sections of these specimens reveal evidence of plastic deformation near the contact surface to a depth of about 20 μm. Significant work hardening occurred in parts of these layers. Fig. 10 shows a sectioned micrograph and a graph of the hardness versus depth profile. The surface hardness of the unworn area of the disc shown in Fig. 10 is about 35 HRC. However, the graph in Fig. 10 shows that the hardness of the near-surface layer has been elevated to 55 HRC in the worn section. The hardness decreases rapidly to about 40 HRC at a depth of 20 μm and continues decrease to about 37 HRC at about 100 μm. Similar hardness tests were performed on a 45 HRC specimen. The hardness–depth profiles for the worn and unworn areas are shown in Fig. 11(a). The results show that the hardness

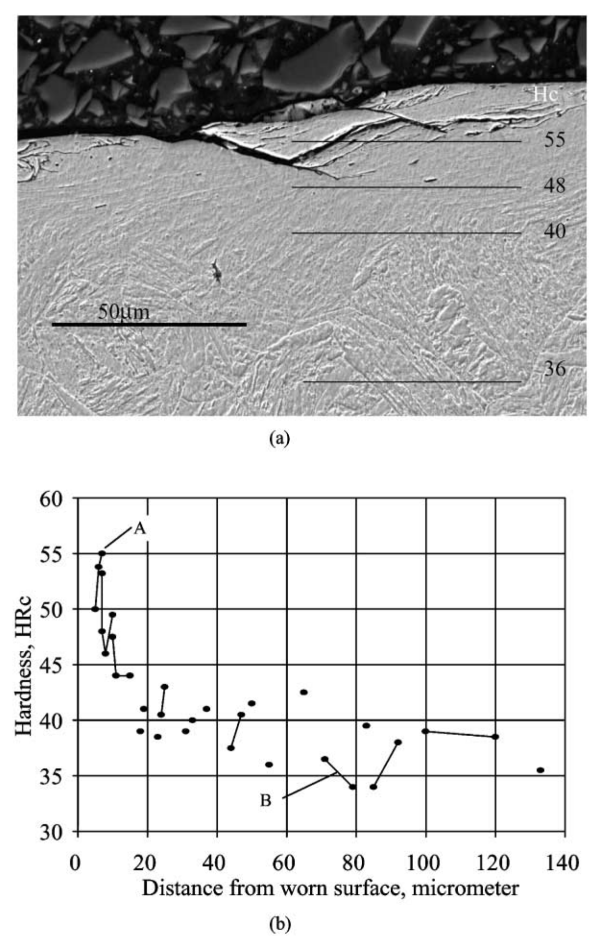

Fig. 10. Hardness–depth profile of the near-surface layer at the wear site on a 410 ss (35 HRC).

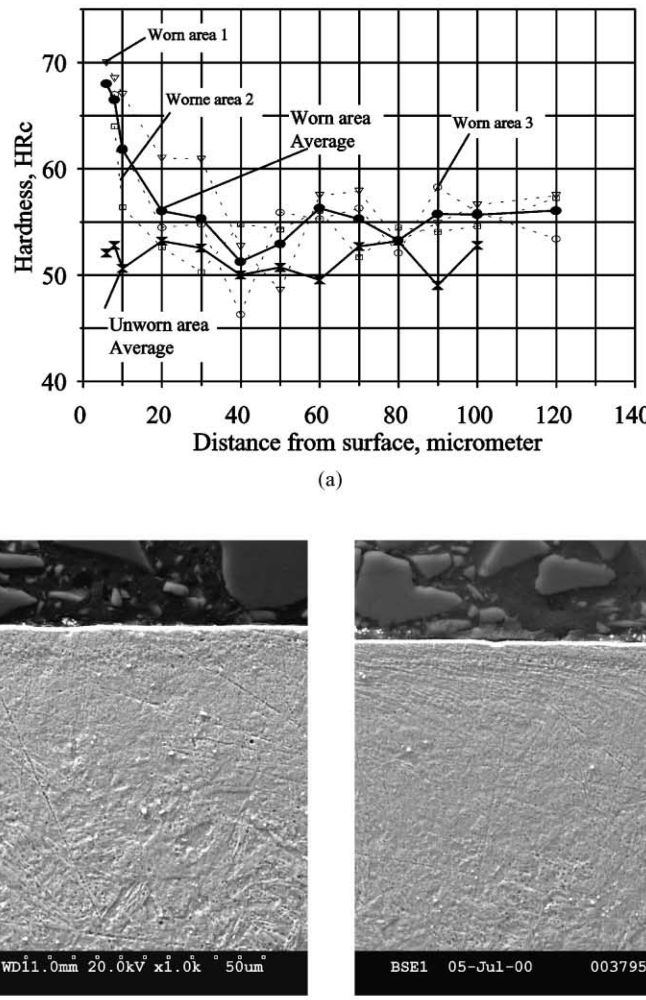

(a)

(b)

(c)

Fig. 11. Hardness–depth profile and micrographs of a 410 ss (45 HRC) worn disc: (a) hardness–depth profile; (b) unworn area, no work hardening; (c) worn area, work hardened.

of the top 20 μm layer has been elevated to 65–70 HRC, and that the hardness of the unworn section remains at around 45–50 HRC from near surface to a depth of 120 μm. It should be noted that the ultra-microhardness tests give a slightly higher reading, 5–10%, than that obtained with a standard Vickers hardness tester. Fig. 11(b) and (c) show, respectively, the cross-section micrographs taken from a worn and an unworn area. Plastic flow near the top 20 μm can be observed clearly in the worn area.

5. Discussion

The present study considers a specific wear mechanism that generates relatively large wear particles from surface micro-cracks under dry sliding conditions. Surface cracks that were in the range of 10–30 μm in length and 10–30° inclination from the surface have been observed from worn specimens. These wear results show that after 60 cycles, the mass losses of the discs are negligibly small. Interestingly, after 720 cycles, the mass losses of the harder discs were higher than the mass losses of the softer discs. It is noted that the harder discs were heat-treated to increase their hardness from 35 to 45 HRC. It was also shown earlier that the hardness of the heat-treated disc was elevated to nearly 70 HRC in the worn surface layer. The heat-treatment and work hardening processes might favour the formation of micro-cracks on the surface and near-surface resulting in the formation of larger particles.

The finite element model for wear particle formation studied the crack parameters within an extended range of crack length (15–50 μm) and crack orientation (15–45°). Previous studies in crack propagation, wear particle formation and detachment presumed the modes of fracture before analysing the contact conditions at the crack faces. The outcome of these assumptions is that the crack faces are closed and the crack face friction prevents tangential movement. Thus, there can be no crack growth. The present study incorporated the ‘contact elements’ in the mixed mode fracture analysis to simulate the actual crack face conditions providing realistically proportioned SIFs for crack growth calculations. The results showed that under certain conditions of loading and initial crack orientation, the crack faces do open and sliding does occur. The crack propagates and turns forming a detached particle. The characteristics of the estimated particles shown in Table 1 appear to be realistic.

The model shows, as expected, that the number of cycles required to form a wear particle and the cross-section shape of the particle are affected by the original crack orientation and crack length. Figs. 5–7 show that the number of cycles needed to generate a particle increases as the normal force is decreased. It was observed that below 340 N, the stress intensity factor obtained for the second load step was below the threshold level of 6.0 MPa $m^{1/2}$ so the crack would cease to grow for that load step.

The model is still empirical in the sense that it assumes the presence of a surface crack of specified length and entry angle. However, with input from statistical analysis of experimental data and finite element analysis of crack growth characteristics, an optimal set of micro-crack parameters can be established. By combining these micro-crack parameters with surface statistics, it is possible to develop an idealised predictive wear model for less ductile materials in dry sliding. For a more realistic model, the rheology of the particle layers needs to be considered and included. The detached particles may be dispersed immediately to complete the wear process resulting in a steady wear rate. On the other hand, these particles may be trapped at the interface and be reworked to form finer particles before dispersal.

6. Conclusions

- A model which incorporates linear elastic fracture mechanics with finite elements has been developed to predict wear particle size for metal surfaces in sliding contact.
- A comparison of the numerical results with laboratory experiments shows that the model predicts realistic results for moderately brittle steel surfaces with fairly high sliding friction.
- The conditions at the crack tip are a changing combination of modes I and II displacements, the relative amounts being found numerically. Some formulas for crack-turn-angle and fracture under combined modes, essential for predicting wear particle size, are shown to agree with experimental results.
- Experimentally, both inclined short-cracks and thin long-cracks that follow the shear-flow were observed. Their presence appears to be related to the hardness of the worn surface layer. The inclined short-cracks give rise to bulkier particles whereas the thin long-cracks give rise to slivers and wear sheets.
- There is evidence of significant work hardening of the worn surface layer; a 40% increase at the near surface up to a depth of 20 μm, compared to the far-field value. This hardening then decays gradually to the far-field value over a total distance of about 40 μm.
- The finite element model showed that the formation of particles and their characteristics are sensible to the applied normal load, initial crack length and crack orientation.

Acknowledgements

This research was supported by grants from the Natural Sciences and Engineering Research Council of Canada (NSERC) and Atomic Energy of Canada Limited (AECL). The authors wish to thank Mr. Mark Robertson at the National Research Council of Canada (NRC) for his assistance in the experimental and metallography work. The computation was carried out in the computing facilities at the University of British Columbia and Babcock and Wilcox Canada.

References

[1] D.A. Rigney, W.A. Glaeser, The significance of near surface microstructure in the wear process, Wear 46 (1978) 241–250.
[2] P.L. Ko, G. Knowles, H. Vaughan, Friction characteristics and the wear process of metal pairs in uni-directional sliding, in: Proceedings of the International Tribology Conference, Vol. 1, Japan, 1995, pp. 181–186.
[3] S. Jahanmir, The relationship of tangential stress to wear particle formation mechanisms, Wear 103 (1985) 233–252.
[4] M.T. Hanson, L.M. Keer, An analytical life prediction model for the crack propagation occuring in contact fatigue failure, Trans. STLE 35 (1992) 451–461.
[5] D.M. Bailey, R.S. Sayles, Effect of roughness and sliding friction on contact stresses, ASME Trans. J. Tribol. 113 (1991) 729–738.
[6] J. Yongqing, Z. Linqing, A full numerical solution for the elastic contact of three-dimensional real rough surfaces, Wear 157 (1992) 151–161.
[7] C. Pitot, L. Vincent, K. Dang Van, N. Maouche, J. Foulquier, B. Journet, An analysis of fretting-fatigue failure combined with numerical calculations to predict crack nucleation, Wear 181–183 (1995) 101–111.
[8] C.-C. Yu, B. Moran, L.M. Keer, A simplified direct method for cyclic strain calculation: repeated rolling/sliding contact on a case-hardened half plane, ASME Trans. J. Tribol. 118 (1996) 329–334.
[9] D.A. Hill, Mechanics of fretting fatigue, Wear 175 (1994) 107–113.
[10] F.A. McClintock, Plastic flow around a crack under friction and combined stress, Fracture 4 (1977) 23–38.
[11] M. Comninou, The interface crack in a shear field, ASME J. Appl. Mech. 45 (1977) 287–290.
[12] L.M. Keer, M.D. Bryant, G.K. Haritos, Subsurface cracking and delamination in solid contact and lubrication, in: H. Cheng, L. Keer (Eds.), American Society of Mechanical Engineers, New York, N.Y., Vol. 39, 1980, pp. 79–85.
[13] S.D. Sheppard, J.R. Barber, M. Comninou, Subsurface cracks under conditions of slip, stick and separation caused by a moving load, J. Appl. Mech. 54 (1987) 393–398.
[14] L.M. Keer, M.D. Bryant, A pitting model for rolling contact fatigue, J. Lub. Tech. 105 (1983) 198–205.
[15] A.F. Bower, The influence of crack face friction and trapped fluid on surface initiated rolling contact fatigue cracks, Trans. ASME 110 (1988) 704–711.

[16] F. Erdogan, G.C. Sih, On the crack extension in plates under plane loading and transverse shear, ASME J. Basic Eng. 85 (1963) 519–525.
[17] G.C. Sih, Strain energy density factor applied to mixed mode crack problems, Int. J. Fract. Mech. 10–13 (3) (1974) 305–321.
[18] P.C. Paris, F. Erdogan, A critical analysis of crack propagation laws, J. Basic Eng. 85 (1961) 528–534.
[19] H. Vaughan, Crack propagation and the PTS criterion for mixed-mode loading, Eng. Fracture Mech. 59 (1998) 393–397.
[20] H. Vaughan, A fracture locus for combined modes I and II displacements, in: M. Croitoro (Ed.), Proceedings of the 1st Canadian Conference on Non-linear Solid Mechanics, Vict., 1999, pp. 486–491.
[21] M.A. Magill, F.J. Zwerneman, Sustained modes I and II fatigue crack growth in flat plates, Eng. Fracture Mech. 55 (1996) 883–899.
[22] T.L. Anderson, Fracture Mechanics Fundamentals and Applications, CRC Press, Boca Raton, Ann Arbor, 1991.
[23] K. Tanata, Fatigue crack propagation from a crack inclined to the cyclic tensile axis, Eng. Fracture Mech. 6 (1974) 493–505.